Journal of Sound and Vibration 329 (2010) 2323–2336

Contents lists available at ScienceDirect

Journal of Sound and Vibration

journal homepage: www.elsevier.com/locate/jsvi

Temperature corrected sensor diagnostics for impedance-based SHM

Benjamin L. Grisso *, Daniel J. Inman

Center for Intelligent Material Systems and Structures, Virginia Polytechnic Institute and State University, 310 Durham Hall Mail Code 0261, Blacksburg, VA 24061, USA

ARTICLE INFO

Article history:
Accepted 6 April 2009
The peer review of this article was organized by the Guest Editor
Available online 14 May 2009

ABSTRACT

Previously, a sensor diagnostics method has been developed for the impedance-based structural health monitoring technique. Impedance techniques utilize piezoelectric patches bonded to the structure of interest for inference of damage. Measuring the slope of piezoelectric susceptance allows unhealthy sensor to be identified. While this sensor diagnostics technique is very useful in detecting damaged sensors bonded to a structure, the method is also susceptible to temperature variations. The object of this study is to accurately provide sensor diagnostics at any temperature. The model developed should be accurate and easy to implement on health monitoring hardware. A frame structure is fabricated to simulate a real structure with complex boundary conditions for experimental testing in various thermal environments. A model predicting piezoelectric susceptance slope at any temperature is generated and validated on the frame structure in an extended temperature range.

1. Introduction

Sensors included in a structural health monitoring system are often affixed to structures as a means of identifying structural defects. However, these sensors are susceptible to damage themselves. Sensor diagnostics is a field of study directed at identifying faulty sensors. While the importance of continuing to develop structural health monitoring systems seems obvious for both critical safety and financial factors, developing sensor diagnostics for these detection systems may be just as important. Sensor diagnostics allow a health monitoring system to infer the integrity of the sensors and separate sensor damage from structural defects.

Many damage detection systems will require a large number of sensors distributed over a structure for effective coverage. Many of these sensors will be required to be in locations exposed to adverse operational and environmental conditions. Even sensors bonded in a protected location have the potential to be damaged with large impacts, collisions, or other unexpected catastrophic events. If a sensor connected to a monitoring system yields no output, either from ambient or external excitation, declaring the sensor to be damaged is a likely conclusion. However, the sensor may be still be partially functional, respond to an excitation signal, and provide what seems like an adequate response even if the sensor has degraded in some way. A sensor with breakage or inadequate bonding, potentially from exposure to some form of solvent, impact events, or even fatigue, may significantly change signal characteristics and lead to false positive or negative damage detection results. To provide the best possible indication of structural integrity, the condition of each sensor should be verified before each measurement is taken.

* Corresponding author. Tel.: +1 540 231 2902; fax: +1 540 231 2903.
E-mail address: begrisso@vt.edu (B.L. Grisso).

0022-460X/$ - see front matter © 2009 Elsevier Ltd. All rights reserved.
doi:10.1016/j.jsv.2009.04.007

Various studies have looked at the influence of the bonding layer on impedance measurements. Most recently, Bhalla and Soh [1] investigated the influence of shear lag through the bonding layer for the electromechanical impedance models of piezoelectric actuation and sensing developed by Crawley and de Luis [2] and Sirohi and Chopra [3], respectively. By incorporating the effects of shear lag loss through the adhesive, and extending the previous models to 2D, Bhalla and Soh [1] reveal that the bonding layer can play a large role in the measured electrical admittance signals. To minimize the influence of the boundary layer in recorded measurements, the authors suggest using a thin layer of an adhesive with a high shear modulus, along with the smallest piezoelectric patch necessary. Bhalla and Soh [1] also identify that the susceptance, or imaginary part of the admittance measurement, is most sensitive to changes in the bonding layer and can be used for identifying debonding. However, this model, as well as other bonding layer models, does not provide a method for detecting bonding defects and only outlines what measurements result from improper bonding.

Saint-Pierre et al. [4] introduced a technique to detect bonding defects in a piezoelectric embedded element by monitoring the electrical impedance. After developing a new model, the modifications to the electrical impedance signal are calculated based on the percentage of unbonded sensor area. Both the model and experimental results reveal that as the bonding defect area becomes larger, the thickness of the piezoelectric resonance becomes sharper and more distinct. In contrast, the amplitude of the host structure resonances is reduced. A delaminated area as small as 1 percent is able to be detected by monitoring the piezoelectric resonance. Giurgiutiu et al. [5] also investigated sensor adhesion for structural health monitoring of aging aircraft. The authors noted that sensor bonding defects are indicated by the increasing of sensor resonances while the structural resonances diminish. While these techniques clearly indicate sensor disbonding, the electrical impedance changes due to sensor breakage are not addressed. The methods also rely on monitoring the resonance of the piezoelectric patch. Any sensor fracture will change the piezoelectric resonant peaks, while structural damage will alter the structural resonant peaks. How to distinguish between sensor breakage, structural damage, and sensor debonding is unclear.

A closed-loop detection scheme is developed by Sun and Tong [6] for piezoelectric debonding in beams. Using Timoshenko beam theory, a model is derived with partially detached actuator and sensor piezoelectric patches to illustrate the influence of sensor debonding on vibrational control of a beam. The control parameters are set such that even a slight (0.1 percent debonding) shift in piezoelectric frequency, presumably due to delamination of the piezoelectric from the structure, will cause the control system to become unstable. An unstable control system is therefore an indicator of an unhealthy bonding condition. While the closed-loop control system is sensitive enough to be destabilized by even a small sensor delamination, the influence structural or sensor damage would have on the control system is not completely addressed.

Bach et al. [7] utilized sensor diagnostics for the impedance method to detect damaged sensors caused by simulated harsh aerospace environments. The piezoelectric sensors were exposed to different conditions, including bonding the sensor to a dirty surface and submerging the sensor in a methyl-ethyl-ketone solvent and hot water. Results indicate that with proper sealant and adhesive, sensor degradation due to these conditions is minimal. However, without the sealant, changes in sensor bonding are revealed by the piezoelectric susceptance. The authors also investigate the changes of the imaginary part of the piezoelectric admittance as a result of temperature variations. Results of this testing indicate that temperature compensation is required for every piezoelectric measurement. Blackshire et al. [8] also investigated bonded PZT sensors in an operational aircraft environment in order to improve the durability of these types of sensors in harsh environments.

Lee and Sohn [9] have investigated the use of Lamb waves to detect the presence of damaged sensors in guided-wave structural health monitoring. Using two time reversal-based indices, piezoelectric debonding is successfully identified. The Lamb wave mode ratio is utilized to estimate PZT cracking. The authors claim these methods are able to discern sensor damage from changes in temperature, but, as of yet, there is no experimental work to support these features being temperature independent. Park et al. [10] also investigated the effect of broken sensors on performing Lamb wave damage location.

Previously, an impedance-based sensor diagnostics model has been developed by Park et al. [10–12], which is based on the single dof impedance method model developed by Liang et al. [13,14]. Liang et al. [14] used a mass–spring–damper system to come up with an expression revealing that the electrical admittance of a PZT patch $Y(\omega)$ is a combination of the structure's mechanical impedance $Z_s(\omega)$ and the electrical impedance of the piezoelectric $Z_a(\omega)$, as show in

$$Y(\omega) = \mathrm{i}\omega\frac{wl}{t}\left[\varepsilon_{33}^{T}(1-\mathrm{i}\delta) - d_{31}^{2}Y_{p}^{E} + \frac{Z_a(\omega)}{Z_a(\omega)+Z_s(\omega)}d_{31}^{2}\hat{Y}_{p}^{E}\left(\frac{\tan\kappa l}{\kappa l}\right)\right], \tag{1}$$

where w, l, and t are the width, length, and thickness of the PZT, ε the dielectric constant of the PZT, δ the dielectric loss factor for PZT, d the piezoelectric coupling constant, and Y_p^E is the complex Young's modulus of the PZT at zero electric field. The subscript 33 indicates that the charge density is along the z-axis, and the superscripts E and T indicate quantities measured at zero electric field and zero stress. κ is the wavenumber of the PZT patch described by

$$\kappa = \omega\sqrt{\frac{\rho}{Y_p^E}}, \tag{2}$$

where ρ is the density of the PZT.

To understand how monitoring the admittance of the PZT works for sensor diagnostics, we can look at the static approximation for the admittance of an unbonded patch (sensor dynamics are neglected) [3].

$$Y_{\text{free}}(\omega) = \mathrm{i}\omega \frac{wl}{t}[\bar{\varepsilon}_{33}^{T}(1 - \mathrm{i}\delta)]. \tag{3}$$

Now, looking at Eq. (1), if we let the mechanical impedance $Z_s(\omega)$ go to infinity, the equation simplifies to

$$Y(\omega) = \mathrm{i}\omega \frac{wl}{t}[\bar{\varepsilon}_{33}^{T}(1 - \mathrm{i}\delta) - d_{31}^{2} Y_{p}^{E}] = Y_{\text{free}}(\omega) - \mathrm{i}\omega \frac{wl}{t}[d_{31}^{2} Y_{p}^{E}]. \tag{4}$$

In most cases, assuming that the mechanical impedance is infinity is not unrealistic as the sensors are generally much smaller compared to the structures they are bonded to. The magnitude of the mechanical impedance of the PZT is generally several orders of magnitude lower than that of the structure, so the PZT mass and stiffness are nearly negligible, especially at lower frequencies. Comparing Eqs. (3) and (4), we can see that the only difference is due to the PZT modulus of elasticity and the piezoelectric coupling coefficient. Thus by bonding the PZT to a structure, we should expect a reduction of the admittance by a factor of $(wl/t)[d_{31}^{2} Y_{p}^{E}]$. It is also interesting to note that these changes only influence the imaginary part of the admittance, or susceptance B.

Xu and Liu [16] modified the model by model introducing a bonding layer shear-lag coefficient. The shear-lag is accounted for by including a single dof dynamic model of the bonding layer between the structure and PZT. Park et al. [15] further add to the model by introducing control parameters to account for sensor breakage and sensor delamination. Each of these models reveals that by observing the susceptance of a PZT, the general health of the sensor can be observed. Experimentally, Overly et al. [17] showed that the slope of the susceptance is directly correlated with the amount of debonding or breakage.

The problem with the sensor diagnostics method, as shown by Overly et al. [17], is that any temperature fluctuations can change the slope of the susceptance just as much as a damaged sensor. A recent study analytically estimated that for a $(70 \times 10 \times 0.1\ \text{mm}^3)$ type 5A PZT patch, a 5.5 °C temperature change yields a 1 percent change in the PZT capacitance [18]. Type 5H PZT has even higher temperature sensitivity. For this reason, a technique needs to be developed to compensate for any temperature variations. Temperature compensation has been used to correct the real part of impedance [19–21], used for damage detection, for temperature, but only one study has looked at temperature changes on the imaginary part of the admittance [17]. The model used to identify damaged sensors developed by Overly et al. [17] is a temperature independent method. However, a limited range of thermal measurements were taken on a plate test structure, which is free of any boundary conditions which may be influenced as a result of a temperature change. Also, while the developed algorithm correctly identifies damaged sensors, each sensor must be compared to the others several times to identify sensors which are statistically different from the group. This algorithm may be computationally taxing to implement on an autonomous hardware system and does not compare each individual sensor to a standard guideline of what a healthy sensor's output should indicate. The research presented here will attempt to address these issues for sensor diagnostics on complex structures in varying thermal environments.

A few studies, including Raghavan and Cesnik [22], have looked at the effect of temperature on guided-wave structural health monitoring. Using experimental results, a model provides a correction for changes in time-of-flight values due to temperature increases and allows for accurate damage location. The main factor leading to the change of arrival time due to temperature variations is a change in the Young's modulus. This same conclusion of the modulus of elasticity being the key parameter in altering the time-of-flight was reached by Grisso et al. [23] when developing a simple temperature correction technique for wave propagation damage location to supplement impedance-based health monitoring.

The work here is an initial attempt to generate a model to separate temperature changes from sensor degradation for impedance-based health monitoring. With the recent emphasis on developing autonomous SHM hardware, this model should be as simple as possible to reduce algorithm power consumption. The method proposed here assumes that temperature readings will be acquired with each impedance measurement.

2. Structure fabrication

Many times while experimentally verifying new SHM methods, a structure is used that allows for easy implementation of damage. Often these structures could be beams or joints with bolted connections which can be loosened or tightened to apply different damage conditions. Other times, attaching magnets can be used as a non-destructive means of simulating damage. However, with loosening and tightening bolts, obtaining repeatable conditions between baseline and damaged states is nearly impossible. While magnets are good for initial impedance sensitivity testing, the structure is not actually damaged. The magnets can be seen as a boundary condition change and will only show up as damage at the lower frequencies of the impedance testing range [24,25].

With the focus of this research being on detecting defective sensors, it seems more desirable than ever to have a repeatable method of inducing damage on the structure of interest. Instead of the traditional bolt loosening, a straight line action clamp is used to replace the standard bolt and nut connector. The clamp chosen is model 602 from DE-STA-CO, which can be seen in Fig. 1.

Fig. 1. The DE-STA-CO 602 straight line action clamp has an 889 N capacity.

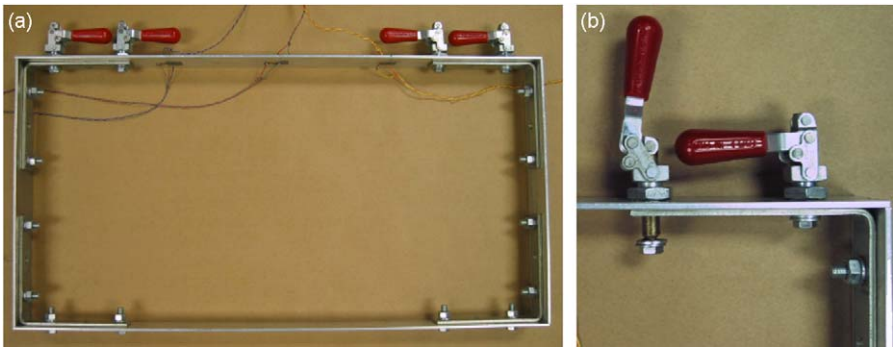

Fig. 2. The completed frame structure (a) and clamping mechanism (b) are shown.

The DE-STA-CO 602 clamp has a handle which moves the plunger forward or backward and locks at either end position. The base of the plunger is threaded to allow the clamp to be mounted to a structure or panel with a jam nut. Also, the plunger is internally threaded, allowing two pieces to be clamped together. The maximum load capacity of the clamp is 889 N.

A frame structure is used to implement the clamps. A 5.08 cm wide, 3.175 mm thick 6063 aluminum beam from National Manufacturing Co. is used to construct a 30.48 cm tall, 60.96 cm wide frame. Corners are connected with 12.7 cm corner angles. Four 0.79 cm diameter, 2.54 cm long (5/16-18 $\times$ 1 in) zinc plated steel bolts with matching nuts and lock washers affix the frame pieces to the brackets at each corner, two on each side of the frame. 0.95 cm through holes are drilled into the frame for each of the bolts. On the top of the frame, the line clamps are used to assemble the frame together instead of bolts.

To attach the clamps, four 1.59 cm wide (5/8-18 in) threaded holes are drilled and tapped into top of the beam. The threads at the base of the clamp plunger are then screwed into the top of the beam and secured with a jam nut. Two clamps are centered in the top beam 3.81 and 11.94 cm from the left end, and two more clamps are placed symmetrically from the right side. A 0.64 diameter (1/4-20 in) hex screw is inserted into each plunger with two washers so that when the clamp is locked with the plunger completely retracted, the top of the frame is attached to the corner angles and, therefore, the rest of the structure. A picture of the completed frame structure can be seen in Fig. 2(a). To show how the clamps attach to the top beam and hold structure together, clamps with their plungers partially extended and completely retracted are shown in Fig. 2(b).

Fig. 3. Clamp 1 (333 N) is on the right of the frame structure.

A frame is chosen for a few reasons. One, the structure has real boundary conditions that will be affected by changes in temperature, as opposed to a free–free beam or plate. These boundary conditions will also affect any piezoelectric material bonded to the structure more than a simple structure. The frame is also more complex than a beam or joint and a realistic representation of a real world structure.

With the clamps either locked to join the beam and angle or unlocked acting as the source of damage to the structure, the repeatability issues of loosening and retorquing a bolt should be avoided. To allow for different levels of damage to the structure, each clamp is set to apply a different force to the structure. The force F that each clamp holds with at its locked position is obtained from

$$F = \frac{\tau}{0.2D}, \tag{5}$$

where τ is the torque place on the screw and D the nominal thread diameter of the screw [26]. To set the clamp forces, each clamp was screwed into the top beam of the structure and secured with the jam nut. The clamp was set to its locked position (right clamp in Fig. 2(b)), and the screws were set to the appropriate torque to obtain the desired force. So, when the clamps are locked, there is a set force, and when the clamps are released, they apply no load to the structure. The clamp force increases with each ascending clamp number. Clamp 1 is set to 333 N, Clamp 2 applies a 445 N force, Clamp 3 is at 556 N, and Clamp 4 is set to 667 N. The clamp positions on the top of the structure can be seen in Fig. 3.

As seen in Fig. 3, Clamp 1, with the lowest preload, is on the right of the structure, and Clamp 4 is on the opposite side. Each of the regular bolts and nuts were tightened to a torque of 2.6 N m (or 1606 N applied force). On all of the threaded surfaces, an epoxy is applied when tightening to prevent loss of preload. Epoxy is used to keep the structure consistent, especially while the structure is expanding and contracting under different thermal loads. The epoxy used is 5 min epoxy gel, a high strength (17.24 N/mm^2 shear tensile), high temperature range (-40 to 93.3 °C) quick setting epoxy from Devcon.

3. Sensor selection

With the structure complete and the clamping forces set, a piezoelectric material needs to be selected to act as self-sensing actuators for the impedance method. The material chosen is a 0.27 mm thick PSI-5H4E material from Piezo Systems, Inc. Square pieces of the PZT, 1.8 cm on a side, are cut to bond to the structure. Before the patches are bonded to the structure, the susceptance for each of the patches in a free–free condition is measured and can be seen in Fig. 4(a). The susceptance is shown in the frequency range from 1 to 20 kHz.

As Fig. 4(a) shows, all of the PZTs are very similar in their unbonded responses. However, as Fig. 4(b) reveals, when enlarging a section of the susceptance, the PZTs are clearly matched in pairs. Each of these pairs of patches will be matched with one being a healthy sensor and one being a damaged sensor. PZTs 4 and 6 become PZTs A and AA, 2 and 5 are now B and BB, and PZTs 1 and 3 are renamed C and CC.

In the frame structure, all of the bolted connections are adhered with epoxy and should be immobile. The only side that should change with damage, and therefore the only side of interest, is the top section with clamps. For this reason, all of the PZTs will be placed on the top section. PZTs are bonded to the beam with cyanoacrylate, and a piece of copper tape affixed to the underside of each PZT allows for leads to be soldered to each patch. PZT A is centered 17.8 cm from the right side of the structure, as shown in Fig. 3. PZT C is bonded 17.8 cm from the left end, and PZT B is placed directly in the center of the top beam. Table 1 displays the names, locations, and damage descriptions for each sensor.

To verify the sensor diagnostics algorithm developed in this research, affixing unhealthy sensors to the structure is also necessary. The rest of the three sensors are attached to the structure with some type of deformity. As these sensors are matched to the first three, they are bonded in the same location as their healthy counterpart but on the underside of the top beam (PZT AA is directly under PZT A, etc.). Each of the three sensors is adhered with a different condition. PZT AA is bonded to the structure normally, but then the top 25 percent of the sensor is broken off to simulate the sensor being struck by a projectile. PZTs BB and CC are both not fully attached to the structure. The top 25 percent of PZT BB is delaminated from the beam, as is the top half of PZT CC. Delamination of a PZT is achieved by placing a piece of release paper under an area the patch to facilitate the desired amount debonding. After the cyanoacrylate bonding the PZT and structure has been mostly cured, the release paper can be removed to allow the patch to be bonded with the appropriate amount of debond. Examples of healthy, broken, and delaminated sensors are illustrated in Fig. 5. A line is drawn on the picture of PZT CC (Fig. 5(c)) to show where the delamination occurs.

With all of PZTs bonded to the structure, the susceptance from 1 to 20 kHz is reacquired. The PZTs are attached to the structure now, so the slope of susceptance will change, and peaks due to structural response will show up in the signatures. Bonded and unbonded susceptance is shown in Fig. 6.

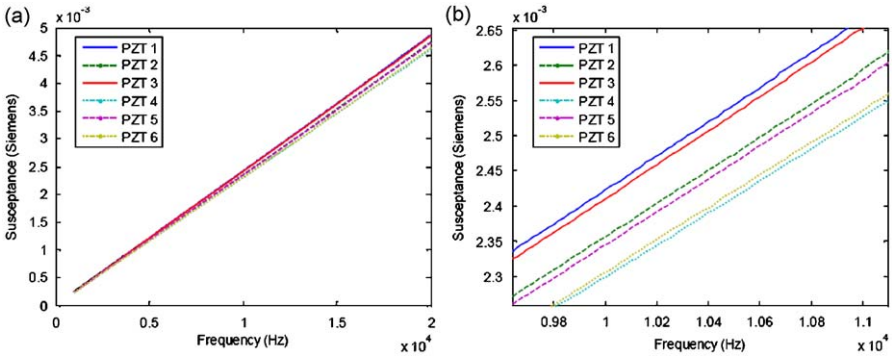

Fig. 4. The free–free PZT susceptances are shown (a), along with an enlarged view (b) to match the PZTs.

Table 1
Descriptions for each of the six PZT sensors are given.

PZT Name	Location (from right of structure) (cm)	Side of top	Damage
A	17.8	Top	NA
B	30.48	Top	NA
C	43.16	Top	NA
AA	17.8	Bottom	25% broken
BB	30.48	Bottom	25% delaminated
CC	43.16	Bottom	50% delaminated

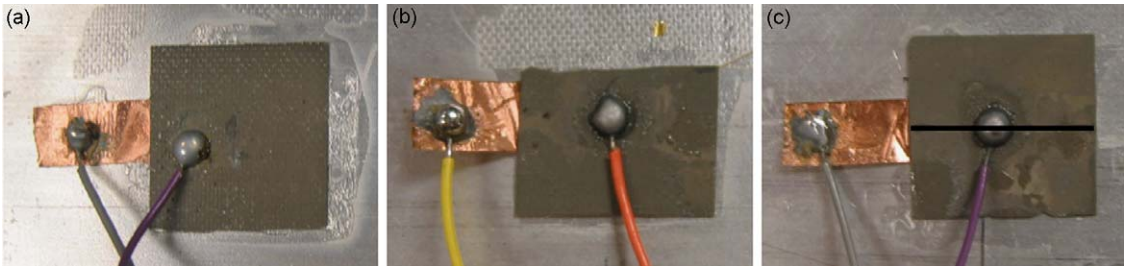

Fig. 5. Images of PZT C—healthy (a), PZT AA—broken (b), and PZT CC—delaminated (c) are shown.

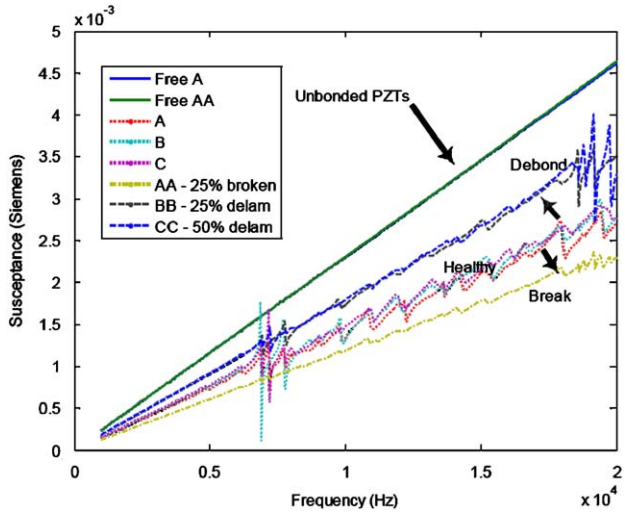

Fig. 6. All six bonded PZTs and two unbonded PZTs are shown to illustrate how sensors affect susceptance.

As expected, Fig. 6 reveals that unhealthy sensors can be detected by the slope of the susceptance. PZT AA, which is 25 percent broken, has a significantly lower slope than the slopes of the healthy sensors. PZTs BB and CC have a larger slope than those of the healthy patches. This higher slope for debonded transducers makes intuitive sense when comparing the slopes to those of the unbonded PZT. As the sensor becomes more and more delaminated, it moves closer to free–free conditions, so the slope should increase. It is expected to see the slope of the susceptance also reflect the extent of the damage to each sensor [17]. No significant difference is seen between PZTs BB and CC. With the difficulty in attaching delaminated patches to a structure, a somewhat imprecise amount of debonding is not entirely unexpected. However, the amount of debonding has already been correlated to the slope of the susceptance [17], and the focus of this research is to simply detect faulty sensor at different temperature levels.

4. Experimental investigations

The completed frame, equipped with both healthy and damaged sensors, is now ready to be tested at temperatures other than room temperature. A limited temperature range from 15 to 65 °C, at 5 °C increments, is decided upon to initially observe the thermal characteristics of the structure and PZT. The whole structure is placed in a Tenney VersaTenn III Environmental Test Chamber, which allows for a controlled temperature and pressure to achieve desired atmospheric conditions. Pressure was maintained at atmospheric conditions for the duration of testing. A picture of the frame viewed through the door on the test chamber is shown in Fig. 7.

As each desired temperature is entered into the test chamber control panel, the chamber is allowed to stabilize for 30 min prior to data acquisition. This time allows the temperature controller and heat exchanger to settle and the contents of the chamber to come to equilibrium. Any temperature fluctuations while testing are generally within a tenth of a degree.

Data is collected with an HP 4194A impedance analyzer. The chamber has testing wires built in to allow the structural PZT to be connected to the impedance analyzer. Using a laptop operating a LabView code, the real and imaginary components of the impedance are collected. A frequency range from 100 to 104,080 Hz is obtained with a frequency resolution of 20 Hz. Medium integration with two averages is used at an excitation amplitude of 1 V. The analyzer can only collect 400 points at a single time, so 13 loops are required to obtain each signature. At each temperature, four impedance signatures are collected for each PZT. With sensor BB and CC being so close to each other in initial slope, only data from PZT CC will be collected (5 PZTs in total). To obtain data useful for sensor diagnostics, the susceptance B is found from the real and imaginary impedance components using the equation

$$B = \mathrm{Im}(Y) = \frac{-X}{R^2 + X^2}, \tag{6}$$

where Y is admittance, X the imaginary component of the impedance, and R the real part of the impedance. The susceptance at 45 °C for all five sensors is shown in Fig. 8.

As Fig. 8 shows, the same basic trend of the susceptance slopes displayed in Fig. 6 holds true for the signatures at 45 °C. The debonded sensor has a higher slope than the healthy sensors, while a lower slope is seen for the broken sensor. These three figures are typical of all signatures for every PZT at each temperature. All signatures generally have very good repeatability amongst the four samples. The curves consistently overlapping without shifting is an excellent indication that the temperature was constant at the chosen level throughout the duration of each test.

As has been previously shown, the slope of the susceptance reveals the health of a sensor bonded to a structure. However, the susceptance slope also changes with temperature. Therefore, a method needs to be in place to determine whether a slope change is due to a type of sensor defect, or whether there is simply a change in the temperature. In the next section, a model will be generated to make this distinction.

Fig. 7. The frame structure is partially viewed through the Tenney Environmental Test Chamber window.

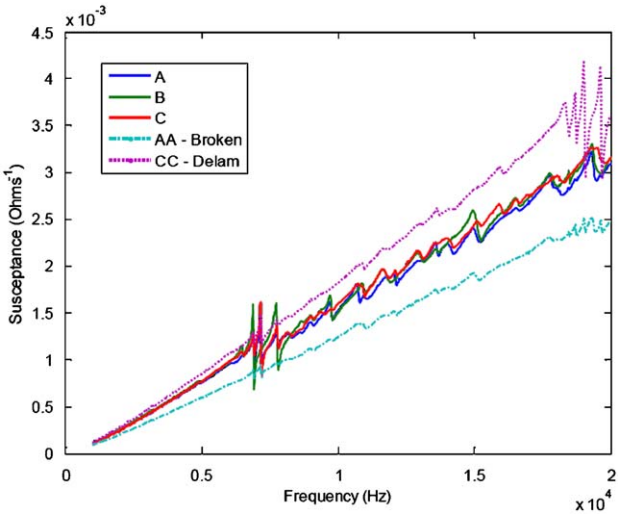

Fig. 8. The susceptance from 1 to 20 kHz for all five sensors is shown at 45 °C.

5. Sensor diagnostics model and algorithm

At every temperature from which data was collected, the susceptance is observed in the range of 1–20 kHz for each PZT. Previous studies have revealed that the slope of the susceptance is linear under 20 kHz, and Eq. (4) is generally considered valid under frequencies of 20 kHz [10–12]. For each sensor, at each temperature, the slope of the susceptance in this range is calculated using a linear least-squares fit ('polyfit' command in Matlab) and recorded. An example of fitting a line to the data for PZT B can be seen in Fig. 9.

After each slope is recorded as described in Fig. 9, the overall trend of the slopes needs to be observed. Plotting the susceptance slope value versus temperature yields an interesting result. For each of the three healthy sensors, the slope of the susceptance is plotted as a function of temperature in Fig. 10.

As Fig. 10 reveals, the slope of the susceptance increases linearly with temperature in the range of 15–65 °C. The only exception seems to be at 15 °C. However, when testing at 15 °C, the test chamber could not maintain a steady temperature, and the temperature readout was often above 15 °C. Thus, for the purposes of modeling, the slopes at 15 °C will not be considered.

With the healthy sensors showing a linear trend of susceptance slope over the initial temperature range, it is expected that the two broken sensors should follow the same pattern. The slope values of the susceptance should be liner, constantly above (debonded) or below (broken) the healthy sensors. Fig. 11 displays the susceptance slope values of the two broken sensors along with the slopes of the healthy sensors.

As expected, the slope of the broken sensor is consistently below the slopes of the healthy sensors. PZT CC, the debonded sensor, shows slope values higher than the healthy slopes susceptance values. PZT AA, the PZT with a 25 percent smaller area than the healthy sensors, has slope susceptance values consistently lower than each of the three healthy sensors for each temperature.

Now it is time to come up with a model to represent the healthy sensors and effectively sort out the broken sensors. This model will need to be implemented on autonomous SHM hardware [27–29], so it is most logical to ensure that the model is as simplistic as possible. When permanently installed on a structure, the hardware should be completely autonomous with all the required operational power being harvested from ambient energy. Any savings in energy from reducing the computational power by keeping the algorithm efficient will help the goal of operating the system with energy harvesting as the sole source of power.

In the case of this structure, it seems that the most obvious solution is to model the slopes of the healthy sensor susceptances versus temperature seen in Fig. 10. Using the same technique to obtain the slopes of the susceptance, the line equations are generated for the three healthy sensors. To generate a single line, the mean of these line equations is used in order to base the model on the expected value of a healthy sensor. The slope of the susceptance S is taken to be

$$S = \mu_m T + \mu_b, \tag{7}$$

where T is the temperature in °C, μ_m the mean of the susceptance slope values, and μ_b the mean of the susceptance slope y-intercepts. This equation is based on the equation for the susceptance values B as described in Fig. 9.

$$B = mf + b, \quad 1000\,\text{Hz} < f < 20,000\,\text{Hz} \tag{8}$$

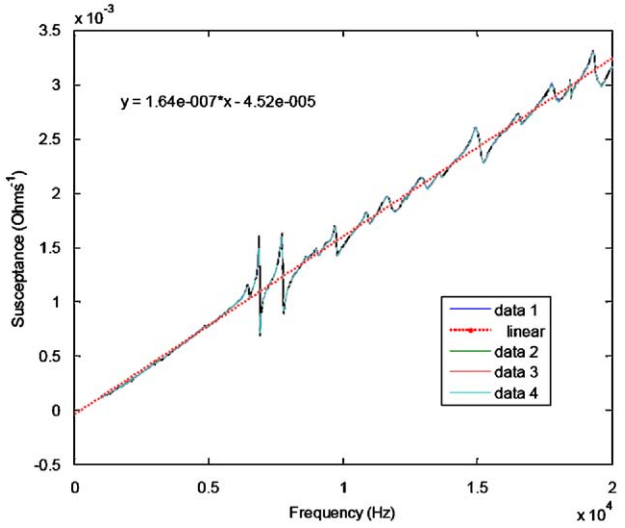

Fig. 9. The slope of susceptance from PZT B at 45 °C is calculated.

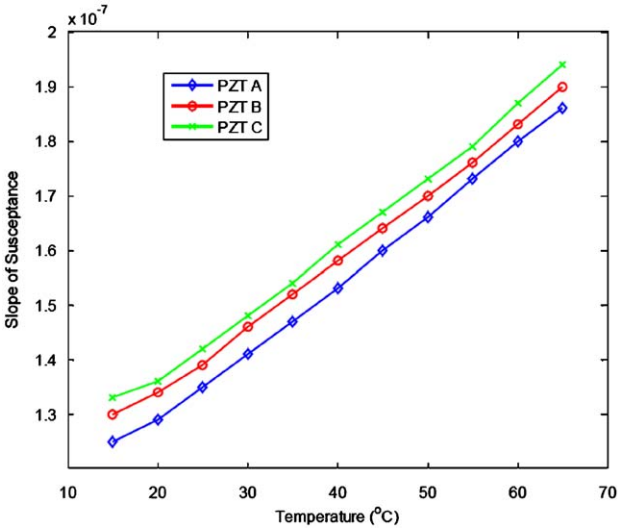

Fig. 10. The slopes for the healthy sensors are shown from 15 to 65 °C.

Here, m is the slope of the susceptance and b the y-intercept value. Obviously this equation does not describe the peaks seen in Fig. 9, but only a straight line describing the expected value between 1 and 20 kHz.

With the expected susceptance slope value for a healthy sensor defined, an expression of an acceptable range for healthy sensors needs to be characterized. A straightforward method of defining the boundaries is simply using the standard deviations of the susceptance slope values and susceptance slope y-intercepts. High S_{high} and low S_{low} susceptance slope boundaries can be described as

$$S_{\text{high}} = (\mu_m + n\sigma_m)T + (\mu_b + n\sigma_b) \tag{9}$$

$$S_{\text{low}} = (\mu_m - n\sigma_m)T + (\mu_b - n\sigma_b) \tag{10}$$

where σ_m is the standard deviation of the susceptance slope values, σ_b the standard deviation of the susceptance slope y-intercepts, and n the number of standard deviations to use.

A model should be defined which describes the expected slope values of a healthy sensor for the frame structure at any temperature. Within some acceptable range, the sensors will be deemed healthy, but outside this range, it is likely the sensors have some sort of defect. Using this newly generated model, the values taken experimentally in Fig. 11 will be used to determine if the model accurately represents what is happening with the structure. Three standard deviations are used ($n = 3$), and the new model and previous experimental values are displayed in Fig. 12.

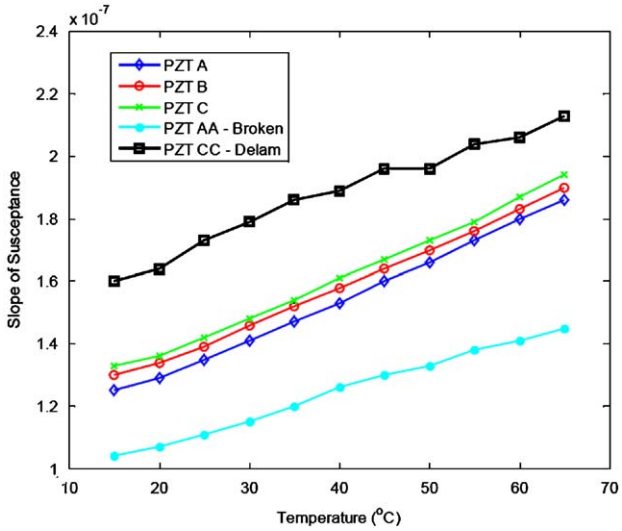

Fig. 11. The slope values for the two broken sensors are added to the healthy slope values of Fig. 10.

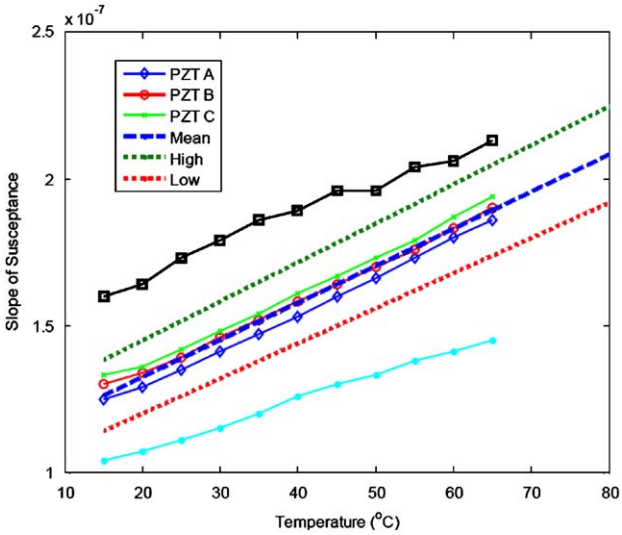

Fig. 12. The model accurately bounds the healthy sensors and identifies the defective sensors.

The model correctly identifies the defective sensors at each temperature. The healthy sensors are bounded with the high and low slope model, and the broken sensors are both well outside of this range even when using three standard deviations. The values generated from this modeling are displayed in Table 2.

With this model based only on experimental data, it is necessary to ensure the accuracy of the results. In this case, the sample variation of the acquired data should not be greater than sensitivity of the model. In Fig. 9, four separate susceptance measurements are shown. All four of the curves sit directly on top of one another and show little, if any, variation. Each of these measurements is also averaged 2 times with the impedance analyzer. So, for each temperature used to create the model, 24 averages are essentially used, with almost no variation among each measurement. This yields a good indication that, in fact, the sensitivity of the model is greater than the sample variation.

A simple and effective model is now in place to detect any defective sensors. Next, it would be desirable to use the sensors on the structure to look for any structural defects. Using broken sensors when looking for damage is not acceptable, therefore, an algorithm is developed to exclude the use of defective sensors in damage detection calculations. This algorithm compares the slope of the susceptance for any acquired measurement to the values given by the model. If the

Table 2
The values used for the susceptance slope model are given.

μ_m	μ_b	σ_m	σ_b
1.264×10^{-9}	1.0703×10^{-7}	2.212×10^{-11}	3.712×10^{-9}

sensor is found to be defective, it will be excluded from any further damage detection use. The algorithm used to simultaneously sort sensors and detect damage is detailed as follows:

1. Enter the temperature. When this algorithm is implemented on hardware, the temperature will be read automatically.
2. Open the data.
3. Find the susceptance from the real and imaginary curves using Eq. (6).
4. Find the slopes of the susceptance for each sensor from 1 to 20 kHz using the linear least-squares approach previously described.
5. Set the number of standard deviations to use when defining the high and low model boundaries.
6. Load the model values defined in Table 2.
7. Find the high and low boundaries using the temperature defined in Step 1.
8. If the susceptance slope for any of the sensors is higher than S_{high}, display 'Sensor is Damaged (Possibly Delaminated)'.
9. If the susceptance slope for any of the sensors is lower than S_{low}, display 'Sensor is Damaged (Possibly Broken)'.
10. If the sensor passes Steps 8 and 9, the damage detection process occurs.
11. Using the root mean square deviation (RMSD) damage metric, real impedance signatures over a specified frequency are compared to a baseline.
12. The real impedance curves and the damage metric values are the displayed in a figure.

The RMSD described in Step 11 is used as a simple method to assess changes in the peaks of the impedance signatures by comparing individual peaks to see how much they changed. The RMSD method for finding the damage metric, M, can be described as

$$M=\sqrt{\sum_{i=1}^{n}\frac{[\mathrm{Re}(Z_{i,1})-\mathrm{Re}(Z_{i,2})]^2}{[\mathrm{Re}(Z_{i,1})]^2}}, \tag{11}$$

where $Z_{i,1}$ is the baseline, or healthy, impedance of the PZT and $Z_{i,2}$ the impedance used for comparison with the baseline measurement at frequency interval i [24]. Before the susceptance slopes are generated, the real impedance for each sensor is plotted to allow the user to detect any potential errors or hardware glitches from the data acquisition.

6. Model verification

Using an initial temperature range from 15 to 65 °C, a model was generated to separate healthy from unhealthy sensors. Debonded sensors will be above the acceptable bounds for a well bonded sensor, and broken sensors will have lower susceptance slope values than the healthy sensors. A model working well in the temperature range it was defined in is expected, but now the robustness of the model needs to be tested in an expanded temperature range.

To verify the model for use over an expanded thermal range, the frame structure was placed back into the environmental test chamber. Again, a HP 4194A impedance analyzer is used to obtain measurements. The data acquisition settings remain the same, but for these experiments, data is only collected from PZTs B, AA, and CC. As with before, an appropriate amount of time is allowed for each temperature to stabilize before the data collection process begins. Three temperature settings, 75, 85, and 95 °C, are used to test the model in an extended range. Fig. 13(a) shows the slope of the susceptance at the new temperatures compared with the previously collected slopes. In Fig. 13(b), the model is generated and plotted over the values.

As Fig. 13(a) shows, the slope of the susceptance at higher temperatures continues to follow the same linear trend as seen at the lower temperatures. Even more noteworthy is that when the model is overlaid with the experimental data (Fig. 13(b)), the slopes at higher temperatures follow the guidelines set by the model. The susceptance slopes of PZT B are well within the acceptable bounds of the model, and are generally close to the expected value of the model. All of the slope values for PZT CC at elevated temperatures are greater than the high boundary, and, likewise, PZT AA slopes are less than the lower model boundary. These results indicate that the simple model generated in the previous section is well suited for sensor diagnostics detection at different temperatures.

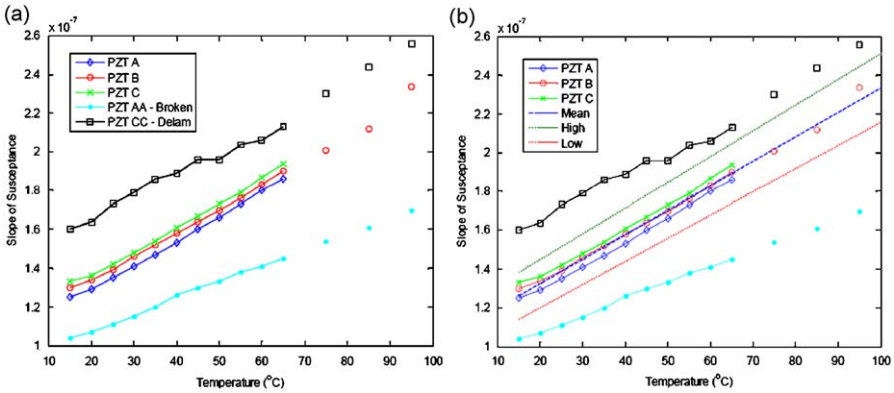

Fig. 13. The susceptance slopes at the new temperatures are shown with the previously collected values (a) and then compared with the model boundaries (b).

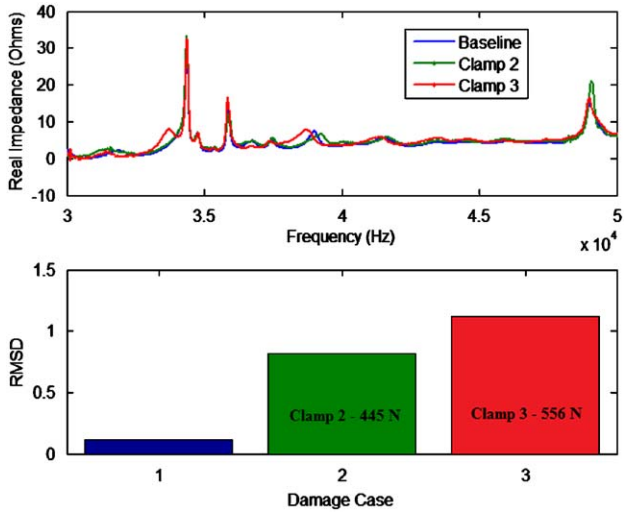

Fig. 14. The real impedance from 30 to 50 kHz and damage metric are shown for PZT B at 95 °C.

7. Model verification with damage

The simple expected value model has proven to be effective at temperatures outside the initial thermal range. With the confidence in the model gained from the testing, the sensor diagnostics and damage detection algorithm is ready to be tested. While data was being collected to verify the model in the previous section, measurements at 75, 85, and 95 °C were also being taken with different damage states.

First, baseline real impedance measurements were taken for each temperature. As with the previous section, PZTs B, AA, and CC are used for this testing. The chamber was then reopened, and Clamp 2 was released. Disengaging the clamp should effectively simulate a loss of bolt preload. To ensure a constant temperature at each damage level for a valid comparison, the frame was brought back up to the desired temperature and allowed to come to equilibrium again before measurements were taken from each signal. The same process is then repeated, but, instead, Clamp 3 is opened and Clamp 2 is locked back into position.

Once all the data is collected, the sensor diagnostics and damage detection algorithm is executed. For this example, the 95 °C data is used, and the number of standard deviations is set to three. The frequency range used for damage detection is set from 30 to 50 kHz based on the presence of several peaks in the impedance signature (indicating strong sensor/structure interaction). Fig. 14 shows the damage detection plot generated automatically by the algorithm.

On the display screen, the algorithm states that PZT CC is possibly delaminated. From Fig. 13(b), this is deemed to be a true statement. Also the algorithm has successfully identified PZT AA as being broken. The output shown in Fig. 14 is the damage detection plot calculated from PZT B, which, in this case, is the only healthy sensor. As seen in the top of Fig. 14, the three real impedance curves lay on top of each other with variations in the peaks due to opening the two clamps. The consistency of the curves indicates that the structural temperature was the same for each test. In the bottom of Fig. 14, the

RMSD values are displayed. The bar colors match up with the corresponding real impedance signature color. The first bar compares two baseline measurements. A low, but non-zero, value is expected due to noise in the measurements. The second bar compares the signature acquired with Clamp 2 open to the baseline, while the third bar shows the comparison of Clamp 3 being open to the undamaged structure. Both of the damaged states are easily detectable. For this structure, a RMSD damage threshold level of around 0.5 seems reasonable. Anything above this level would likely be detected as damage. Also assuring is that the damage due to Clamp 3, with a greater force, is higher than that of Clamp 2.

For each of the other two temperatures, similar results were generated. The algorithm correctly excluded the two damaged PZTs from the damage detection process. Also, the results of the damage detection remained the same, with the damage metric value for Clamp 3 being open greater than that for Clamp 2. Both of these damaged conditions are easily identifiable from the non-damaged state. For the frame structure, both the expected value model and the algorithm generated are very effective at temperatures within and outside of the initial model thermal range. With this model being effective on a structure with complex boundary conditions, it stands to reason that this type of sensor diagnostics modeling could work for any number of real world structures subject to varying temperatures below the Curie temperature of the piezoelectric.

8. Conclusions

In this paper, a technique to separate temperature variations from sensor defects is presented for the impedance-based structural health monitoring technique. A frame structure is fabricated to simulate a real structure with complex boundary conditions for experimental testing in various thermal environments. The frame is equipped with locking clamps to provide a consistent method for applying damage. Three healthy and three damaged PZT patches are attached to the structure.

After acquiring impedance measurements in an initial limited temperature range, a model is developed to separate damaged from healthy sensors. The model is based solely on healthy sensor readings and temperature measurements. An algorithm is then formed using the model to exclude damage sensors from participating in damage detection on the structure. Experimental verification of the model and algorithm in an extended temperature range correctly identified damaged sensors, carried out damage detection with the healthy sensors, and provided damage identification of the host structure.

In addition to validating and generating a model, the experimental results have also revealed that measured susceptance slope is linearly related to changes in temperature. This relation could prove to have a number of future benefits, including simplicity in temperature compensation and modeling and an alternative method for temperature monitoring with limited sensors. Perhaps the greatest advantage of this temperature influenced sensor diagnostics method is the simplicity of the model. Only a few values need to be stored for the algorithm to be implemented on autonomous hardware. Obviously, temperature measurements will need to be included with the acquisition of each impedance signature. Adding temperature readings to hardware systems will only require a low amount of power dissipation.

Acknowledgments

The authors would like to thank Dr. Gyuhae Park from Los Alamos National Laboratory for his assistance with this research. This material is based upon work supported by the National Science Foundation under Grant no. 0426777.

References

[1] S. Bhalla, C.K. Soh, Electromechanical impedance modeling for adhesively bonded piezo-transducers, *Journal of Intelligent Material Systems and Structures* 15 (2004) 955–972.
[2] E.F. Crawley, J. de Luis, Use of piezoelectric actuators as elements of intelligent structures, *AIAA Journal* 25 (1987) 1373–1385.
[3] J. Sirohi, I. Chopra, Fundamental behavior of piezoceramic sheet actuators, *Journal of Intelligent Material Systems and Structures* 11 (2000) 47–61.
[4] N. Saint-Pierre, Y. Jayet, I. Perrissin-Fabert, J.C. Baboux, The influence of bonding defects on the electric impedance of a piezoelectric embedded element, *Journal of Physics D: Applied Physics* 29 (1996) 2976–2982.
[5] V. Giurgiutiu, A.N. Zagrai, J. Bao, Piezoelectric wafer embedded active sensors for aging aircraft structural health monitoring, *Structural Health Monitoring* 1 (2002) 41–61.
[6] D. Sun, L. Tong, Closed-loop based detection of debonding of piezoelectric actuator patches in controlled beams, *International Journal of Solids and Structures* 40 (2003) 2449–2471.
[7] M. Bach, C.-P. Fritzen, B. Eckstein, H. Speckmann. Self-diagnostic capabilities of piezoelectric transducers using the electromechanical impedance, *Proceedings of the Sixth International Workshop on Structural Health Monitoring*, Stanford, CA, September 2007, pp. 1931–1938.
[8] J.L. Blackshire, S. Martin, A. Cooney, Characterization and modeling of bonded piezoelectric sensor performance and durability in simulated aircraft environments, *Proceedings of Third European Workshop on Structural Health Monitoring*, Granada, Spain, July 2006.
[9] S.J. Lee, H. Sohn, Reference-free piezoelectric transducer self-diagnostics for structural health monitoring applications, *Proceedings of the Sixth International Workshop on Structural Health Monitoring*, Stanford, CA, September 2007, pp. 1947–1954.
[10] G. Park, C.R. Farrar, F. Lanza di Scalea, S. Coccia, Performance assessment and validation of piezoelectric active sensors in structural health monitoring, *Smart Materials and Structures* 15 (2006) 1673–1683.
[11] G. Park, C.R. Farrar, A.C. Rutherford, A.N. Robertson, Piezoelectric active sensor self-diagnostics using electrical impedance measurements, *International Conference on Adaptive Structures and Technologies*, Bar Harbor, ME, October 2004.
[12] G. Park, C.R. Farrar, A.C. Rutherford, A.N. Robertson, Piezoelectric active sensor self-diagnostics using electrical admittance measurements, *Journal of Vibration and Acoustics* 128 (2006) 469–476.

[13] C. Liang, F.P. Sun, C.A. Rogers, Coupled electromechanical analysis of adaptive material system—determination of actuator power consumption and system energy transfer, *Journal of Intelligent Material Systems and Structures* 5 (1994) 12–20.
[14] C. Liang, F.P. Sun, C.A. Rogers, An impedance method for dynamic analysis of active material system, *Journal of Vibration and Acoustics* 116 (1994) 121–128.
[15] S. Park, G. Park, C.-B. Yun, C.R. Farrar, Sensor self-diagnostics using a modified impedance model for active sensing-based structural health monitoring, *Proceedings of the Sixth International Workshop on Structural Health Monitoring*, Stanford, CA, September 2007, pp. 1923–1930.
[16] Y.G. Xu, G.R. Liu, A modified electro-mechanical impedance model of piezoelectric actuator–sensors for debonding detection of composite patches, *Journal of Intelligent Material Systems and Structures* 13 (2002) 389–396.
[17] T.G.S. Overly, G. Park, C.R. Farrar, Development of signal processing tools and hardware for piezoelectric sensor diagnostic processes, *Proceedings of SPIE's 12th International Symposium on NDE for Health Monitoring and Diagnostics*, Vol. 6530, San Diego, CA, March 2007.
[18] G.E. Simmers Jr., J.R. Hodgkins, D.D. Mascarenas, G. Park, H. Sohn, Improved piezoelectric self-sensing actuation, *Journal of Intelligent Material Systems and Structures* 15 (2004) 941–953.
[19] G. Park, K. Kabeya, H. Cudney, D.J. Inman, Impedance-based health monitoring for temperature varying application, *JSME International Journal* 42 (1999) 249–258.
[20] G. Park, Assessing Structural Integrity Using Mechatronic Impedance Transducers with Applications in Extreme Environments, PhD Dissertation, Virginia Polytechnic Institute and State University, 2000.
[21] K.-Y. Koo, S. Park, J.-J. Lee, C.-B. Yun, D.J. Inman, Impedance-based structural health monitoring considering temperature effects, *Proceedings of SPIE's 12th International Symposium on NDE for Health Monitoring and Diagnostics*, Vol. 6532, San Diego, CA, March 2007.
[22] A. Raghavan, C.E.S. Cesnik, Studies on effects of elevated temperature for guided-wave structural health monitoring, *Proceedings of SPIE's 12th International Symposium on NDE for Health Monitoring and Diagnostics*, Vol. 6529, San Diego, CA, March 2007.
[23] B.L. Grisso, D.J. Leo, D.J. Inman, Temperature influences on the wave propagation technique for use in supplementing impedance-based structural health monitoring, *Proceedings of SPIE's Ninth International Symposium on NDE for Health Monitoring and Diagnostics*, Vol. 5394, San Diego, CA, March 2004, pp. 222–232.
[24] G. Park, H. Sohn, C.R. Farrar, D.J. Inman, Overview of piezoelectric impedance-based health monitoring and path forward, *The Shock and Vibration Digest* 35 (2003) 451–463.
[25] F. Bouteiller, B.L. Grisso, D.M. Peairs, D.J. Inman, Broken rail track detections using smart materials, *Proceedings of SPIE's 11th International Symposium on NDE for Health Monitoring and Diagnostics*, Vol. 6178, San Diego, CA, February 2006, pp. 65–75.
[26] R.C. Juvinall, K.M. Marshek, *Fundamentals of Machine Component Design*, third ed., Wiley, New York, 2000.
[27] B.L. Grisso, D.J. Inman, Autonomous hardware development for impedance-based structural health monitoring, *Smart Structures and Systems* 4 (2008) 305–318.
[28] J. Kim, B.L. Grisso, D.S. Ha, D.J. Inman, A system-on-board approach for impedance-based structural health monitoring, *Proceedings of SPIE's 14th International Symposium on Smart Structures and Materials*, Vol. 6529, San Diego, CA, March 2007.
[29] B.L. Grisso, J. Kim, J.R. Farmer, D.S. Ha, D.J. Inman, Autonomous impedance-based SHM utilizing harvested energy, *Proceedings of the Sixth International Workshop on Structural Health Monitoring*, Stanford, CA, September 2007, pp. 1373–1380.